Contents lists available at ScienceDirect

Earth and Planetary Science Letters

journal homepage: www.elsevier.com/locate/epsl



The presence of silicate melt may enhance rates of cation diffusion in olivine



Thomas Shea a,*, Dawn Ruth b, Michael Jollands c, Kenta Ohtaki d, Hope Ishii d, John Bradlev d

- ^a Department of Earth Sciences, University of Hawai'i at Mānoa, HI, United States
- ^b U.S. Geological Survey, California Volcano Observatory, Menlo Park, CA, United States
- ^c Gemological Institute of America, New York, NY, United States
- d Hawai'i Institute of Geophysics and Planetology, University of Hawai'i at Mānoa, Honolulu, HI, United States

ARTICLE INFO

Article history: Received 1 June 2023 Received in revised form 4 August 2023 Accepted 25 August 2023 Available online xxxx Editor: C.M. Petrone

Keywords: diffusion chronometry olivine crystal chemistry magmatic timescales silicate melt

ABSTRACT

Olivine is commonly used as a 'crystal clock' to extract timescales relevant to pre-eruptive perturbations within mafic magmatic systems. Diffusion chronometry applications require accurate calibrations for the rates at which Fe-Mg or other commonly measured elements like Ni, Mn, and Ca diffuse through the crystal lattice. In the past, these rates have been mainly characterized using solid-solid diffusion couple experiments involving olivine single crystals, thin films, or powder sources. Despite the presence of melt surrounding olivine in natural magmatic systems, very few experiments involving magma have been performed, largely because controlling interface reactions is difficult. For this study, we carried out olivine-melt diffusion experiments as a test of the diffusion chronometry method, and to determine whether the presence of melt influences the calculated timescales. To approximate a natural system, we incorporated small natural Kīlauea and San Carlos olivine seeds within a natural Kīlauea basalt and tracked diffusive re-equilibration through time. To better control interface reactions, after some equilibration period at an initial superliquidus temperature of 1290°C, the runs were rapidly cooled to form a rim and left to dwell at various final temperatures (1200, 1220, 1240, 1255°C) for 6-84 h. Concentration gradients for Fe-Mg, Mn, Ni, Ca were measured, and the step-wise nature of the core-rim transition was ascertained using slow diffusing elements like P or Al. When these gradients are modeled using published diffusivities, the timescales retrieved are typically 10 times longer than the actual experiment durations. Thus, measured diffusivities are an order of magnitude faster than those previously obtained in olivine-solid source experiments, but they are in excellent agreement with the only two other melt-olivine datasets. We explore reasons for why melt-bearing olivine diffusion experiments tend to yield faster rates. The possible effects of (1) growth during diffusion, (2) diffusion during any initial dissolution step, and (3) extended tube or planar defects at the interface on calculated diffusivities are all considered but found to be inconsequential. Instead, we argue that additional point defects (vacancies) are likely created at the interface by higher concentrations in elements like Al or H in the basalt melt compared to other solid couple diffusant sources. Future applications of diffusion chronometry in olivine may require a complete re-evaluation of published diffusivities using melt-bearing experimental configurations.

© 2023 Elsevier B.V. All rights reserved.

1. Introduction

Magmatic processes responsible for volcanic eruptions on Earth (e.g., magma ascent, exsolution, crystallization, recharge/mixing) often result in thermodynamic disequilibrium. This disequilibrium catalyzes mineral-melt reactions, where crystals grow or dissolve

* Corresponding author. E-mail address: tshea@hawaii.edu (T. Shea). and/or re-equilibrate with a new environment via diffusion of its chemical components. Olivine (Fe,Mg)₂SiO₄ can preserve valuable records of the processes responsible for disequilibrium in mafic-tointermediate magmas, in the form of chemical zoning in both major (Fe-Mg), minor (Ni, Ca, Mn) or trace elements (e.g., Cr, P, Al, H) (Costa et al., 2008). Interface reactions (e.g., rapid skeletal growth) also cause partial or full trapping of melt pockets in olivine hosts, which can be interrogated for information on pre-eruptive magma chemistry as well as storage pressures (e.g., Kent, 2008; Wallace

et al., 2021). In addition, relaxation of chemical zoning within a zoned olivine or in melt inclusions provides critical time information via diffusion chronometry: if elemental diffusion rates are well constrained, concentration gradients can be exploited to obtain the duration between a pre-eruptive thermodynamic perturbation and quenching at the surface. Because elements often diffuse at different rates, many chronometers can be leveraged within a single olivine crystal (e.g., Chakraborty, 2008; Costa et al., 2020). Olivine is also structurally and chemically simpler than other minerals, with one tetrahedral site occupied mainly by Si⁴⁺ (and to a minor extent other pentavalent and trivalent elements P5+, Al3+, Cr³⁺, Fe³⁺), and two different octahedral sites M1 and M2 largely occupied by divalent cations (Fe²⁺, Mg²⁺, Ca²⁺, Mn²⁺, Ni²⁺). Applications of diffusion chronometry in olivine have been soaring over the last two decades (see Costa et al., 2020), particularly as experimentally-derived cation diffusivities became increasingly well calibrated and point defect models refined (Nakamura and Schmalzried, 1983; Chakraborty, 1997, 2010; Petry et al., 2004; Coogan et al., 2005; Ito and Ganguly, 2006; Demouchy and Mackwell, 2006; Holzapfel et al., 2007; Dohmen and Chakraborty, 2007; Dohmen et al., 2010). Diffusion timescales obtained using Fe-Mg. Ca, Ni, and Mn diffusion in olivine from various eruptions of basaltic to andesitic magma form the vast majority of the available dataset. Those timescales are now frequently compared and correlated with pre-eruptive gas and geodetic and seismic timeseries to gain a more integrated understanding of the timing of magmatic unrest (Kahl et al., 2013; Longpré et al., 2014; Albert et al., 2015, 2019; Pankhurst et al., 2018; Ruth et al., 2018; Rasmussen et al., 2018; Viccaro et al., 2019; Caracciolo et al., 2021). In most cases, diffusion timescales are interpreted in the framework of magma mixing, where the olivine cargo is suddenly placed in different melts, experiences disequilibrium and often interface reactions, and subsequently re-equilibrates diffusively until eruption. Ensuring that timescales extracted from diffusion chronometry are accurate requires ensuring that cation diffusion rates are accurately determined in the first place.

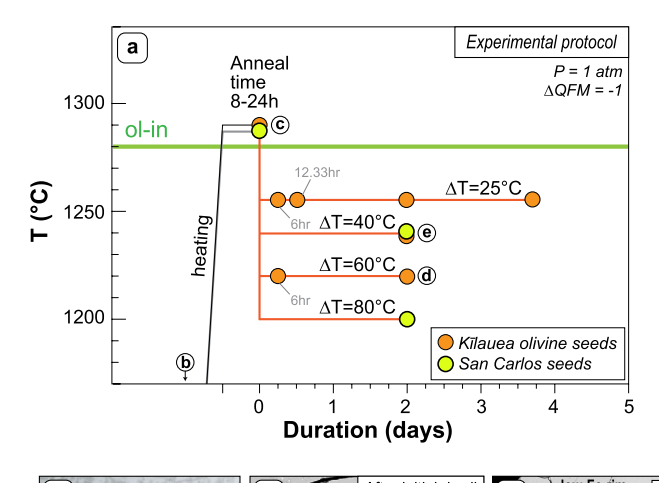
Diffusivities of Fe-Mg, Ca, Ni, and Mn have been generally well quantified as a function of temperature (T), pressure (P), oxygen fugacity (fO_2), major element composition of the olivine (X_{Fo}), crystallographic direction (a, b, or c-axis), and to a lesser degree, as a function of water fugacity (fH_2O , Hier-Majumder et al., 2005). Yet the experiments exploited to calibrate the diffusivity expressions adopted by diffusion chronometry studies (Fe-Mg, Dohmen and Chakraborty, 2007; Ni, Holzapfel et al., 2007; Ca, Coogan et al., 2005; Mn, Chakraborty, 2010) were all performed using solid-solid couples (powder source, thin films or polished and oriented olivine pairs). In natural magmatic systems, olivine is surrounded by silicate melt. Changes related to the presence of melt compared to olivine-only are expected to relate mainly to the activity of SiO₂ (aSiO₂) (e.g., Zhukova et al., 2017). However, differences in aSiO₂ are relatively minor between a basaltic melt and olivine compared to aSiO₂ differences imposed in Zhukova et al. (2017) using the periclase- or orthopyroxene-olivine systems, and not expected to strongly influence cation diffusivities. Nevertheless, the two other studies focused on olivine-melt couples by Jurewicz and Watson (1988) and Spandler and O'Neill (2010) yielded element diffusivities (including rare earth elements, see Cherniak, 2010) that were higher than their solid-solid counterparts. These results were not fully understood and are still the subject of significant debate. One of the main drawbacks of employing melt-olivine couples for diffusion studies involves interface reactions. Because olivine may grow or dissolve during these types of experiments, the interface position of a diffusion model used to invert for diffusivity is mobile (Lasaga, 1982). Spandler and O'Neill (2010) circumvented this problem by using cylindrical olivine crucibles and precisely determined olivine-basalt equilibrium to avoid growth or dissolution.

In this study, we set out to test whether more nature-like diffusion couple configurations involving basaltic melt surrounding olivine yielded element diffusivities that were consistent with previous studies. Specifically, the experiments presented herein test the simple premise that olivine bathed in new, non-equilibrium melts can re-equilibrate diffusively and yield accurate timescales using diffusion chronometry based on available solid-solid diffusivity data. In essence, this experimental study provides a first order groundtruthing of diffusion chronometry applications in individual olivine grains within natural magmas. We show that contrary to expectations, applying diffusion chronometry to our experiments with current literature values for diffusivities yields timescales that are about an order of magnitude slower than real experimental timescales. We discuss the possible reasons for this discrepancy and the consequence for durations extracted from crystal clocks. We advocate for further melt-bearing experiments with well-controlled geometric configurations to confirm these results.

2. Materials and methods

The conceptual framework simulated by our experiments is as follows: olivine crystals from a natural starting material are placed in sudden thermodynamic disequilibrium, and their diffusive reequilibration with the surrounding melt is tracked with time. The melt consists of high-Mg (MgO = 11.4 wt.%) tholeiitic basaltic powder from an 1820-23CE Kīlauea eruption, with an olivine cargo that is often more magnesian (\sim Fo₈₆₋₉₀, Lynn et al., 2017) than its host melt (at equilibrium with $Fo_{86-86.5}$, Shea et al., 2022). The starting material was derived from coarsely crushed, vitric 'golden pumice' with less than 10 vol.% olivine (Garcia et al., 2003). Large (> 0.5 mm) olivine phenocrysts were separated from the crushed natural basalt to obtain a relatively homogeneous glassy starting material. Two approaches were then adopted (Fig. 1). First, a series of charges incorporated 1-5 olivine phenocrysts in the starting basalt powder to replicate a scenario where natural olivine with a prior history was placed in a basalt melt at a temperature that would induce disequilibrium. In this case, disequilibrium was brought about by raising the initial temperature in a 1-atm gas mixing furnace to above the olivine liquidus (1290°C, Shea et al., 2019), resulting in partial phenocryst dissolution. Subsequently, charges were cooled rapidly to final temperatures of 1200-1255 °C, inducing growth of an olivine rim, and then left to dwell at the final conditions for durations of 6-84 h. The advantage of this first approach is that it broadly simulates a realworld magma mixing scenario. However, this configuration cannot allow complete separation of zoning associated with diffusive reequilibration from potentially pre-existing zoning (despite the partial dissolution step). A second approach therefore involved placing large (> 2 mm) olivine seeds sourced from San Carlos or the same Kīlauea starting material after manually removing at least 25% of the broken crystal and rounding the edges. While individual San Carlos olivine grains are not zoned (Lambart et al., 2022), grinding the outer portions from large Kīlauea crystals removes any potentially zoned rims. Another advantage of using large olivine seeds is that concentration gradients formed by diffusion will be a tiny fraction (here, $< 150 \mu m$) of the total radius of the seed (several mm). This configuration helps mitigate any interface curvature or dimensional effects highlighted in Shea et al. (2015) (see section III in the Supplementary Material for details).

Experiments were all carried out at fO_2 conditions buffered at 1 log unit below the quartz-fayalite-magnetite reaction curve (QFM-1), using a mixture of H_2 and CO_2 (Mourey and Shea, 2019; Shea et al., 2019). These fO_2 conditions are within the range investigated by other solid-solid diffusion studies (e.g., Dohmen and Chakraborty, 2007). Olivine seeds were placed in globs of basalt powder and polyvinyl alcohol glue, roughly shaped into a bead



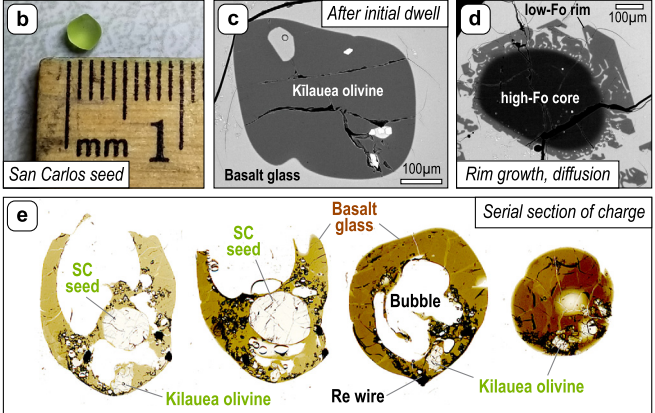


Fig. 1. (a) Experimental protocol (modified from Shea et al., 2019). The experimental charges containing Kīlauea phenocryst seeds and/or San Carlos olivine seeds (b) are heated to an initial temperature slightly above the olivine liquidus to prevent growth and favor slight dissolution. (c) They are annealed for 8–24 h at 1290 °C, before being cooled to final temperatures between 1200 and 1255 °C and left to dwell at these final conditions for 6–84 h before (d) and (e) being quenched. A number of these experiments are from Shea et al. (2019) and Mourey and Shea (2019), see Methods section for details.

around a coiled Re wire loop. The other side of the Re loop was attached to a Pt hanger at the end of a holder alumina rod and placed inside the 1-atm furnace at temperatures of 600-700 °C. Temperature was then ramped up to the initial superliquidus conditions at a rate of 240 °C/h. After 8-24 h of anneal time at these superliquidus conditions, charges were cooled by turning off element power (cooling time to final conditions < 4 min) and left at the final temperatures for various durations before quenching. Quenching involved melting the thin Pt hanger wire so that the molten beads fell into a water-filled beaker underneath the furnace. The beads were then recovered, impregnated in a small recipient of epoxy, and serial-sectioned 3-5 times to ensure maximum probability of intersecting a target phenocryst/seed more than once. The exposed surfaces of each section displaying the largest phenocryst sections were mounted and polished for electron microprobe analysis.

Electron microprobe analyses were performed according to analytical setups already presented in Shea et al. (2019). Most olivine concentration profiles were acquired using a 20 keV accelerating voltage, a 250 nA current, a spot size of 1–5 microns and an element setup consisting of Si, Mg, Al, Fe, Cr, Mn, Ni, Ca, P. For a subset of these profiles, only Si, Mg, Fe, Ca, and Ni were analyzed. Calibration standards included San Carlos and Springwater olivine (Si, Fe, Mg), Verma garnet (Mn), Kakanui augite and Durango apatite (Ca, P), plagioclase (Al), chromite (Cr), and NiO (Ni) standards. Analytical precision is < 10% for P, < 5% for Al, < 3%

for Cr, Mn and Ni, < 2% for Ca, and < 0.5% for Si, Mg, and Fe. Concentration profile data are available as Supplementary Material. X-ray intensity maps of Mg, Al, P, Ca, Ni were acquired for a small subset of experimental olivine to verify that the boundary between slow- (Al, P) and fast- (Fe-Mg, Mn, Ni, Ca) diffusing elements differed and showed sharp gradients for the slow diffusing elements. Importantly, Ca concentration profiles likely suffer from fluorescence effects, leading to apparent increases in Ca at the olivine rims (e.g., Gavrilenko et al. 2023). No corrections were attempted, meaning that Ca diffusivities obtained suffer from greater uncertainty. Nonetheless, we choose to report both profiles and calculated diffusivities for completeness in case robust corrections can be applied in the future.

Diffusion modeling on resulting concentration profiles was carried out by considering two distinct scenarios: First, under the assumption that the olivine rims grew around a partially dissolved, unzoned seed, an initial step-wise profile was constructed, matching changes in concentration shown in Al and/or P when those elements were analyzed. "1-step" diffusion models were then fit to the observed Fe-Mg, Ni, Ca, Mn and Cr profiles (note: not all elements were analyzed in every crystal) (a) to determine timescales using diffusivity expressions published in the literature and test whether they matched with experimental timescales, or (b) to determine element diffusivities from the known experimental duration. In this first set of models, the dwell at the final conditions (after rim growth) were chosen as the appropriate comparative timescales. Second, after observing that diffusive re-equilibration had occurred in some resorbing seeds at the initial conditions (i.e., diffusion exceeding the pace of dissolution, see results below), we carried out additional "2-step" diffusion models. During the first step, we assumed that resorption at the future core-rim interface effectively stopped, and that diffusive re-equilibration happened during the initial 8-24 h at 1290 $^{\circ}$ C. Then, in a second modeling step, those initial, partially re-equilibrated seeds grow a rim nearly instantaneously (e.g., Mourey and Shea, 2019) and diffusion proceeds in a fashion similar to the 1-step models presented above. The boundary conditions and modeling procedures are detailed in the Supplementary Material. The figures and tables in the main text report results pertaining to the 1-step models. The influence of including multiple steps is further examined in the discussion. Because temperatures, pressures, fO2, experimental times were well controlled and a high precision analytical routine was used, uncertainties in calculated diffusivities or timescales were mainly associated with profile fitting assumptions relating to the position of the initial core-rim interface. To account for profile asymmetry associated with a significant compositional dependence of diffusion (particularly for Fe-Mg, Ni, Mn), we allowed the interface to be moved one distance node towards the rim or core to obtain better fits to the profiles (Matano-type interface). This choice resulted in a maximum of two-fold changes in timescales or diffusivities. Therefore, we conservatively report timescales or diffusivities as best-fit values with a total range covering 4-fold variations.

We also carried out electron backscatter diffraction (EBSD) analyses on the experimental olivine to determine their orientation in thin section and allow characterization of diffusion anisotropy. Data were collected on the Tescan Vega 3 scanning electron microscope with an attached Oxford Symmetry EBSD detector located at the U.S. Geological Survey Menlo Park, CA USA. Column conditions were set to 15–20 kV with a 17.5–20 mm working distance. Beam intensity (effectively beam current) was set to optimize the Kikuchi pattern but not saturate the image (17–19 on Tescan). Unique solutions were obtained with a Hough resolution between 45 and 60, and a minimum of 9 resolved Kikuchi bands. Finally, the solution was acceptable if the mean angular deviation was less than 1°. The raw data were post-processed using the automated "cleaning" feature in Aztec Crystal 2.0, which removed wild spikes and

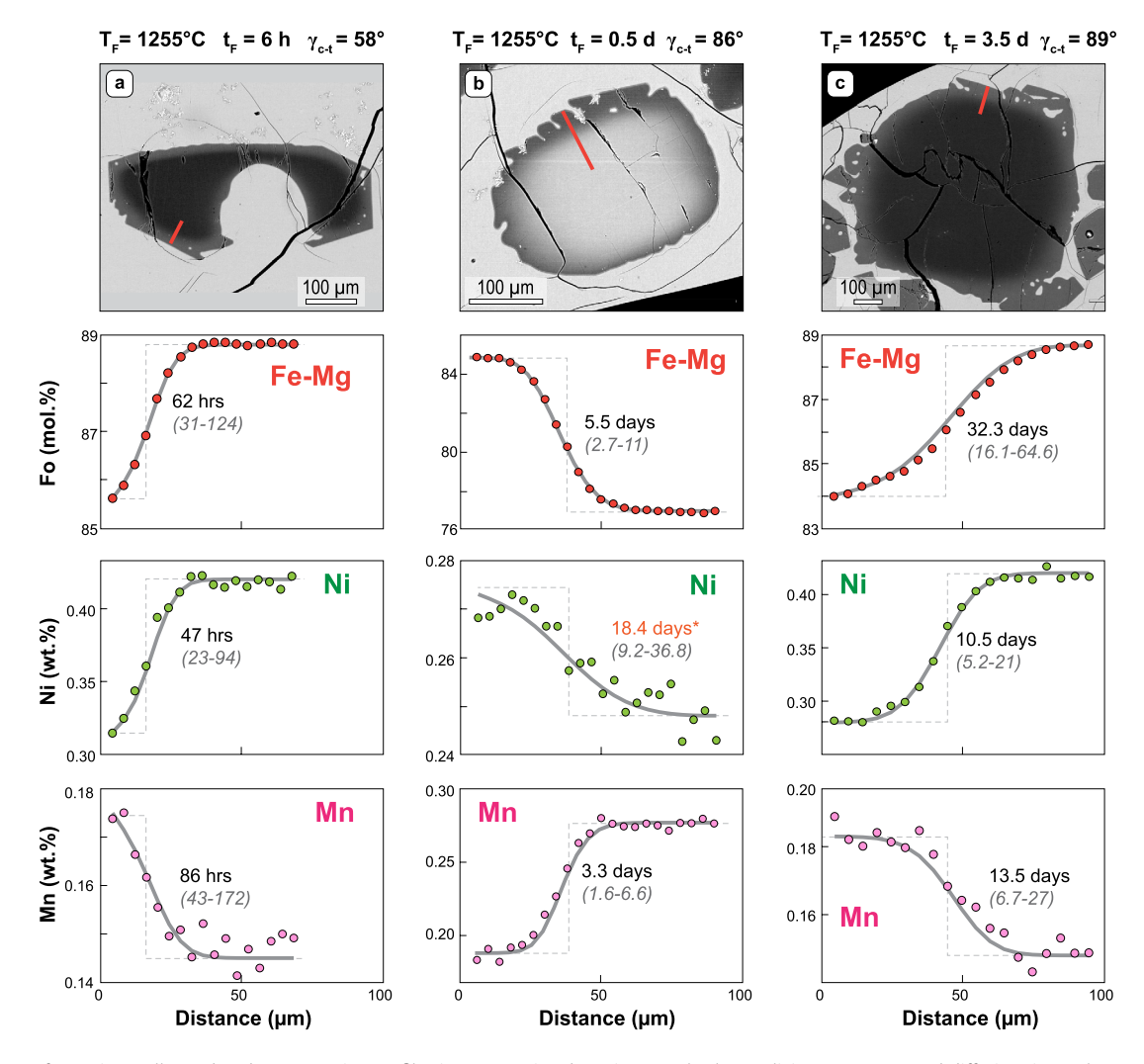


Fig. 2. Three sets of experimentally-produced concentration profiles in Fe-Mg, Ni and Mn in natural Kīlauea olivine at 1255 °C, and diffusion timescales retrieved assuming diffusivities available in the literature (Dohmen and Chakraborty, 2007; Chakraborty, 2010). These experiments involved no grinding of crystal rims prior to the run (see Methods for details). (a) Profile oriented 58° from the c-axis after 6 h of diffusion in normally-zoned olivine phenocryst yields best-fit timescales between 47-86 h. (b) Profile in reversely-zoned olivine after 12 h of diffusion yields best-fit timescales of 3.3-18.4 days (asterisk denotes a less well-resolved analytical profile for Ni). (c) Normally-zoned olivine after 84 h of diffusion, with calculated timescales of 10.5-32.3 days. Timescales in parentheses show the maximum allowable range given a 4-fold uncertainty associated with diffusion modeling assumptions.

zero solutions. The traverse-crystallographic axes angles are summarized in the Supplementary Table, and the full EBSD map data with Euler angles is available as a compressed Supplementary Material file.

Lastly, two experiments were imaged using transmission electron microscopy to try and resolve planar defects that may be present between a partially resorbed olivine core and overgrowth rim, as well as at the interface between olivine and basalt glass. An electron-transparent thin section of each olivine, 100–150 nm thick, was produced using a Helios 660 dual-beam focused ion beam SEM (FIB-SEM, FEI Co.) instrument with an Oxford Instruments XMaxN 80 silicon drift detector system at the Advanced Electron Microscopy Center at the University of Hawai'i at Mānoa. The FIB section was then characterized by employing 300 kV brightfield imaging and high-resolution lattice-fringe imaging using a 60–300 kV high-base Titan G2 analytical (scanning) transmission electron microscope (TEM/STEM, FEI Co.).

3. Results

The subset of experimental olivine mapped for cation zoning shows that, as expected (e.g., Spandler and O'Neill, 2010; Chakraborty, 2010), gradual concentration gradients in Fe-Mg, Ni,

Ca, and in many cases Cr, formed between cores and rims (Figs. 2, 3, 4 and Table 1). By contrast, slower diffusing elements like P and Al showed sharp step-wise gradients. We therefore concluded that the experimental protocol was successful in creating sharp interfaces between dissolution and growth, and that gradual changes in surrounding melt composition during dwell times at the final composition were likely minor compared to the instantaneous perturbation caused by imposing sudden undercooling (Shea et al., 2022)

Using published diffusion coefficients to calculate timescales from experimentally-produced gradual concentration profiles in Fe-Mg, Ni, Mn – and to a smaller subset of profiles of Ca and Cr – from rim to core resulted in durations that are systematically overestimated (Figs. 2, 3). The true experimental dwell times at final conditions are shorter by factors of $5-20\times$ (Fe-Mg), $2-21\times$ (Ni), $4-24\times$ (Mn), $5-65\times$ (Ca), or on average, by about an order of magnitude (Figs. 3, 4). These results assumed that olivine seeds were either unzoned at the start (San Carlos olivine) or dissolved sufficiently to remove any prior existing zoning at the rim (Kīlauea phenocrysts). Examination of olivine seeds quenched at superliquidus initial conditions (1287 and 1290 °C) prior to cooling revealed a number of grains that were indeed homogeneous

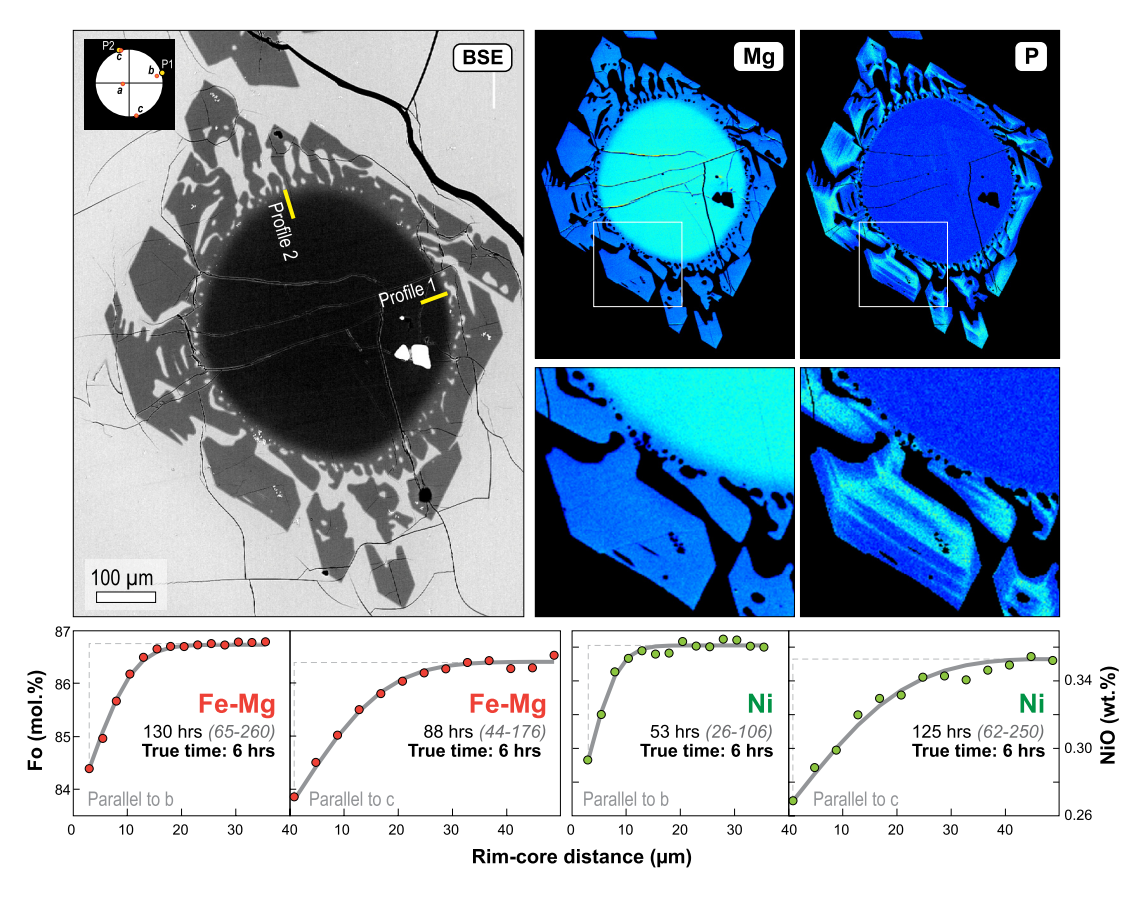


Fig. 3. Set of two mutually perpendicular analytical profiles in Fe-Mg and Ni within experimental olivine (originally, natural Kīlauea seeds) left to dwell at $1220\,^{\circ}\text{C}$ ($-\Delta T = 60\,^{\circ}\text{C}$) for 6 h. Profiles were selected in areas without large overgrowth rims to avoid moving boundary problems in the diffusion models. Grey dashed lines represent initial concentration profiles. Diffusion timescales are retrieved assuming diffusivities available in the literature (Dohmen and Chakraborty, 2007; Chakraborty, 2010) (true experimental time in parentheses). X-ray maps in fast (e.g., Mg) vs. slow (e.g., P) diffusion elements enable verification of the position of the interface between crystal dissolution and re-growth. Overall, best-fit timescales extracted by modeling Fe-Mg and Ni diffusion are \sim 9–21 times longer than the true experimental durations. Timescales in parentheses show the maximum allowable range given a 4-fold uncertainty associated with diffusion modeling assumptions.

Table 1Summary of experimental conditions and calculated cation diffusivities (see Supplementary Table for more details).

Experiment	Start T (°C)	Dwell @ start T (h)	End T (°C)	Dwell @ End T (h)	D_{Fo} $\left(\frac{\text{m}^2}{\text{s}}\right)$	D_{Ni} $(\frac{\text{m}^2}{\text{s}})$	D_{Ca} $\left(\frac{\text{m}^2}{\text{s}}\right)$	D_{Mn} $(\frac{m^2}{s})$	D_{Cr} $(\frac{\text{m}^2}{\text{s}})$
k1820-ol4	1290	24	1255	48	1.7E-15	8.3E-16	6.2E-16	1.6E-15	_
k1820-ol15	1290	24	1255	84	7.9E-16	3.1E-16	2.9E-16	3.4E-16	_
k1820-ol16	1290	24	1255	6	1.3E-15	1.2E-15	3.3E-15	1.8E-15	_
k1820-ol18	1290	24	1255	12.33	1.6E-15	9.0E-16	1.1E-15	9.2E-16	-
k1820-ol18	1290	24	1255	12.33	1.4E-15	1.9E-15	2.8E-15	-	-
k1820-ol18	1290	24	1255	12.33	1.1E-15		2.6E-15	7.3E-16	2.3E-16
k1820-ol20	1290	24	1220	6	9.5E-16	4.5E-16	8.5E-16	-	-
k1820-ol20	1290	24	1220	6	3.9E-15	6.3E-15	_	-	-
k1820-ol20	1290	24	1220	6	8.9E-16	7.0E-16	2.1E-15	1.1E-15	
k1820-ol23	1290	24	1290	0	3.5E-15	2.6E-15	_	-	-
k1820-ol25	1290	8	1240	48	4.4E-15	3.9E-15	5.1E-16	2.3E-15	6.0E-15
k1820-ol25	1290	8	1240	48	4.3E-15	5.3E-15	6.3E-16	3.6E-15	5.7E-15
k1820-ol25	1290	8	1240	48	3.3E-16	2.6E-16	2.6E-16	5.6E-16	1.9E-16
k1820-ol25	1290	8	1240	48	4.8E-16	4.2E-16	2.9E-16	4.5E-16	3.4E-16
k1820-ol26	1290	8	1240	48	5.8E-16	4.4E-16	_	-	-
k1820-ol26	1290	8	1240	48	5.8E-16	3.6E-16	2.8E-16	-	-
k1820-ol26	1290	8	1240	48	2.8E-15	1.6E-15	3.6E-16	-	-
k1820-ol26	1290	8	1240	48	2.7E-15	2.1E-15	5.8E-16	2.0E-15	
k1820-ol27	1287	24	1287	0	1.2E-15	-	2.9E-16	1.6E-15	1.7E-15
k1820-ol31	1290	24	1200	48	3.1E-16	2.5E-16	1.7E-16	-	-
k1820-ol31	1290	24	1200	48	1.9E-15	1.6E-15		-	-
k1820-ol31	1290	24	1200	48	2.9E-16	-	2.8E-16	_	-
k1820-ol31	1290	24	1200	48	1.2E-15	9.1E-16	3.5E-16	-	-

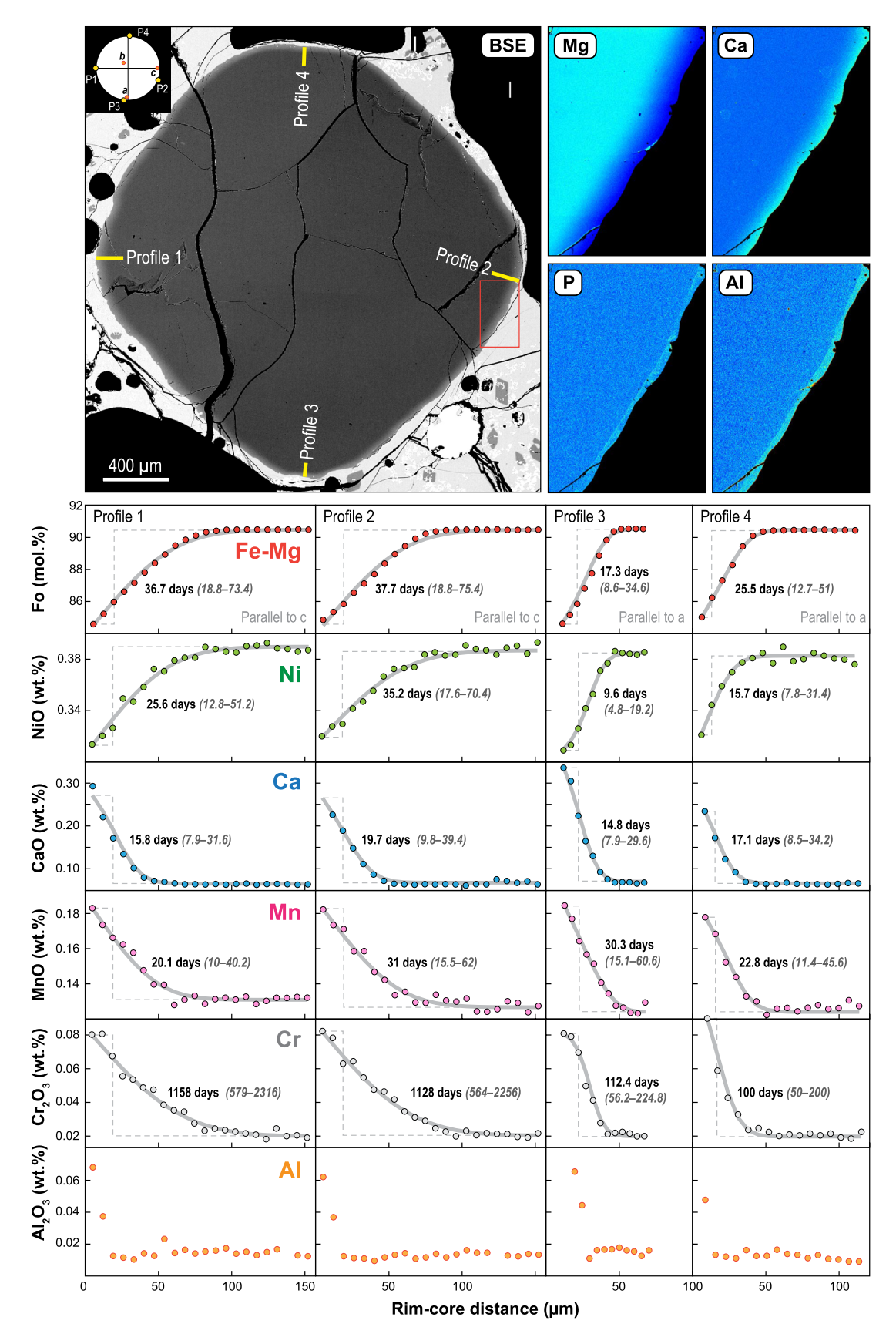


Fig. 4. Diffusion within a San Carlos olivine seed (k1820_ol25) after 48 h at 1240 °C. Two complementary, mutually perpendicular sets of Fe-Mg, Ni, Ca, Mn, Cr, and Al concentration profiles were completed along orientations close to the a and c crystallographic axes. Best-fit diffusion timescales extracted vary between \sim 10 and 38 days for most elements except for Cr (100–1160 days). Timescales in parentheses show the maximum allowable range given a 4-fold uncertainty associated with diffusion modeling assumptions. Within the spatial resolution of the profile, Al shows a sharp concentration gradient. Upper right X-ray maps show the clear difference between fast (Fe-Mg, Ca) and slow diffusing (P, Al) elements. The latter mark sharp contrasts between the core and rim of the seed.

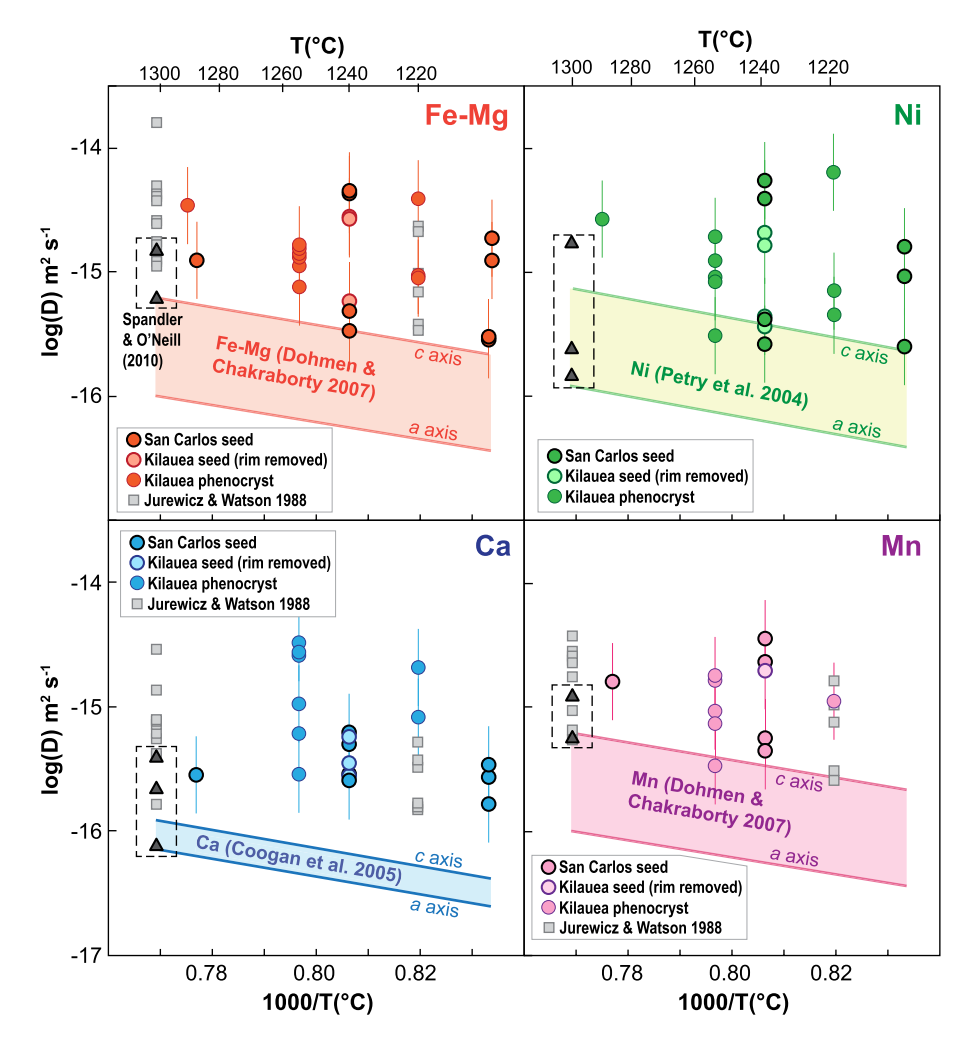


Fig. 5. Diffusivities of Fe-Mg, Ni, Ca and Mn in experimental olivine. In all cases, values calculated are much larger than those predicted by commonly-used expressions (colored fields bound by thick lines). In contrast, our values match well the ranges obtained by other studies that utilized melt-olivine couples, particularly those from Jurewicz and Watson (1988). Vertical error bars account for uncertainties in modeling carried out to extract diffusivities and cover a range of 0.6 log units.

in composition, but others that exhibited concentration gradients even before growth of a rim (Figs. A1 and A2). This zoning appeared even in large San Carlos seeds known to be initially unzoned. Thus, rates of dissolution in some cases were slower than rates of diffusion. This observation is at odds with our predictions based on published diffusion rates, which anticipated formation of at most $\sim 10~\mu m$ diffusive gradients under the assumption of no dissolution. In the discussion section, we consider in more detail how zoning in the initial olivine seeds before cooling, formation of a rim and diffusive-equilibration between seed and rims could affect our results.

Diffusivities calculated from fitting the same profiles yield values that are on average about $10\times$, $7.5\times$, $9\times$, $10\times$ faster for FeMg, Ni, Mn and Ca (Figs. 5 and 6). Our data spans the same range as Fe-Mg, Mn, and Ca data from Jurewicz and Watson (1988), and largely overlaps with that of Spandler and O'Neill (2010). While the olivine-melt diffusivities are almost an order of magnitude higher for most cations, their anisotropic behavior is consistent overall with olivine-olivine (solid-solid) data. Fe-Mg and Mn diffusivities are about $6\times$ higher along the c-axis than along the a or b-axis, matching prior findings (Chakraborty, 2010) (Fig. 7). Ni diffusivities can be fit by accounting for a \sim $10\times$ anisotropy, slightly higher than the $6\times$ anisotropy obtained by Petry et al. (2004). Ca diffusivities also span an order of magnitude, without showing a consistent orientation-dependence (Fig. 7). Part of this variability may be associated with fluorescence effects at the edge of the

concentration profiles. By contrast, fluorescence has little effect on Fe-Mg, Ni and Mn.

4. Discussion: making sense of discrepant experimental results

The cation diffusion rates obtained from our olivine-melt diffusion experiments are in disagreement with those obtained in studies that employed solid-solid couples (powder source, thin films, or olivine couples). The discrepancy is of nearly an order of magnitude for the few elements investigated. Faced with such unexpected results, we discuss next experimental caveats and alternative explanations for why our experiments yield higher diffusivities. The following hypotheses are considered:

Hypothesis 1. Diffusivities are higher in appearance only because our models do not account for growth-induced zoning.

Hypothesis 2. Diffusivities are higher in appearance only because diffusive gradients are already present after the initial superliquidus anneal.

Hypothesis 3. Diffusivities are enhanced by the presence of growth- or dissolution-related planar defects.

Hypothesis 4. Diffusivities are enhanced by the chemistry of the surrounding melt, which modifies the point defect population of the olivine.

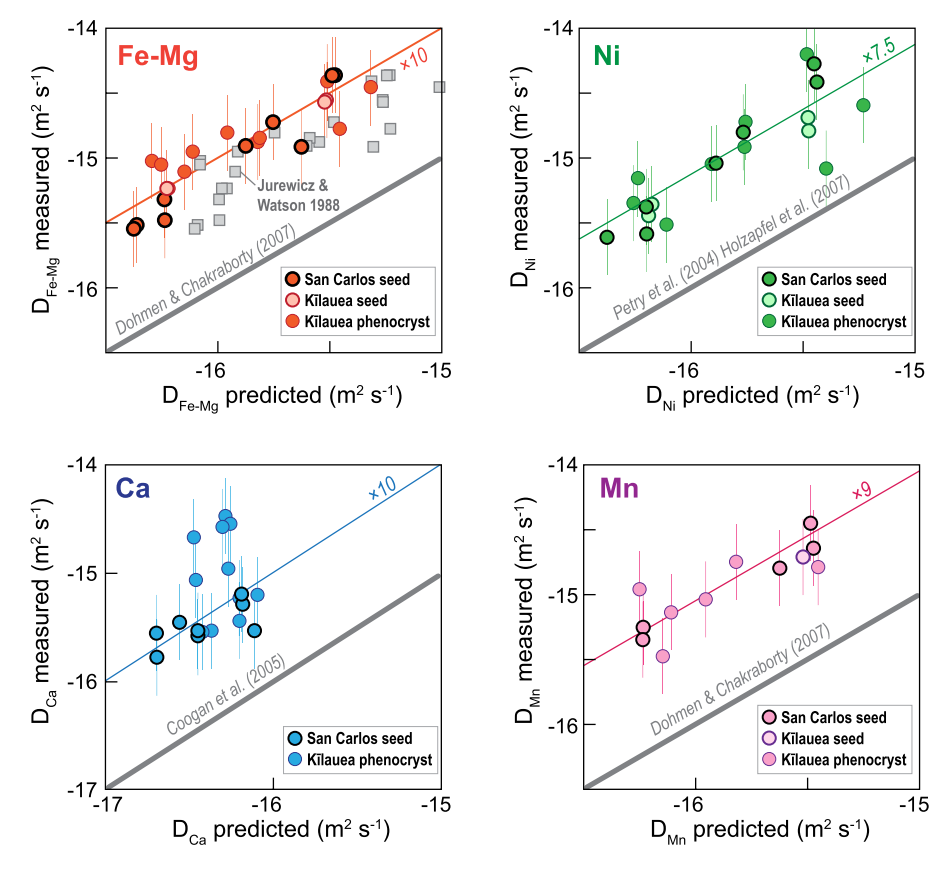


Fig. 6. Measured vs. predicted diffusivities of Fe-Mg, Ni, Ca and Mn in experimental olivine. For the four elements examined, measured diffusivities are roughly $7.5-10 \times$ greater than the values predicted by commonly used expressions. Vertical error bars account for uncertainties in modeling carried out to extract diffusivities and cover a range of 0.6 log units.

4.1. Hypothesis 1: diffusivities are higher in appearance only because models do not account for growth-induced zoning

Olivine seeds experience disequilibrium both during the initial anneal phase and during cooling at the final temperatures. As in most diffusion chronometry applications, the modeling assumes that the rims formed abruptly (timescale of crystal growth « diffusion timescale), creating a step-like concentration gradient between core and rim. If instead the timescales of rim development and intracrystalline cation diffusion are comparable, concentration gradients produced would be the result of a combination of both processes. The rim would at least partially record the evolving melt composition as undercooling is being relieved. Modeling diffusion only along a core-rim transect affected by both growth and diffusion would lead to diffusivity overestimates (Costa et al., 2008). Two lines of evidence argue against significant contribution of growth to generating gradual changes in concentration: (a) A study by Mourey and Shea (2019) showed that much of the growth occurs in < 1 hr in experiments that used the same starting material and cooling strategy. (b) The sharp boundaries identified in slowdiffusing elements like Al or P in X-ray maps indicate that olivine immediately started growing rims with strongly contrasting compositions, and that they did not record a progressive change in surrounding melt composition over the experimental timescales. Shea et al. (2022) also showed that non-seeded crystals that nucleated and grew in some of the same charges showed little to no Fe-Mg zoning. We therefore conclude that the higher diffusivities we obtained cannot be the consequence of growth contributions to zoning.

4.2. Hypothesis 2: diffusivities are higher in appearance only because diffusive gradients are already present after the initial superliquidus anneal

To investigate the extent to which concentration gradients developed by diffusion during the initial anneal step at superliquidus temperature, we quenched two experiments after 24 h at the starting conditions. Despite initial expectations that gradients in Fe-Mg longer than $\sim 10 \mu m$ should not develop according to diffusivities (Dohmen and Chakraborty, 2007) and dissolution rates (Chen and Zhang, 2008) available in the literature, olivine grains within the two benchmark runs (one Kīlauea seed and one San Carlos seed) showed variably zoned Fo profiles (see Supplementary Table). Some gradients reached up to 40 µm along the c axis, while others were far more restricted (10 µm or less), indicating that dissolution rates competed with diffusion rates to variable extents. To further quantify the possible effect of diffusion at the superliquidus anneal stage, we re-modeled concentration gradients in the olivine that had undergone annealing, cooling and rim growth assuming two separate steps: A first step involved diffusion at the initial high temperature (1290 °C) conditions, taking diffusivities extracted from the San Carlos benchmark experiment (k1820_ol27), and a second step involved diffusion at the lower temperatures (1200-1255 °C). The boundary conditions for the initial superliquidus treatment were taken by fitting straight lines through plots of Fo, Ni, Mn, Ca vs. T - including data on newly grown olivine from Shea et al. (2022) - yielding equilibrium rim compositions of Fo_{86} , NiO = 0.36, CaO = 0.25, MnO = 0.17 wt.% respectively (see for example Supplementary Fig. A3). The two-step models gave slightly lower diffusivities globally, on average by factors of 1.86×, 1.44×, 1.93× for Fe-Mg, Ni, and Mn respectively (maximum dif-

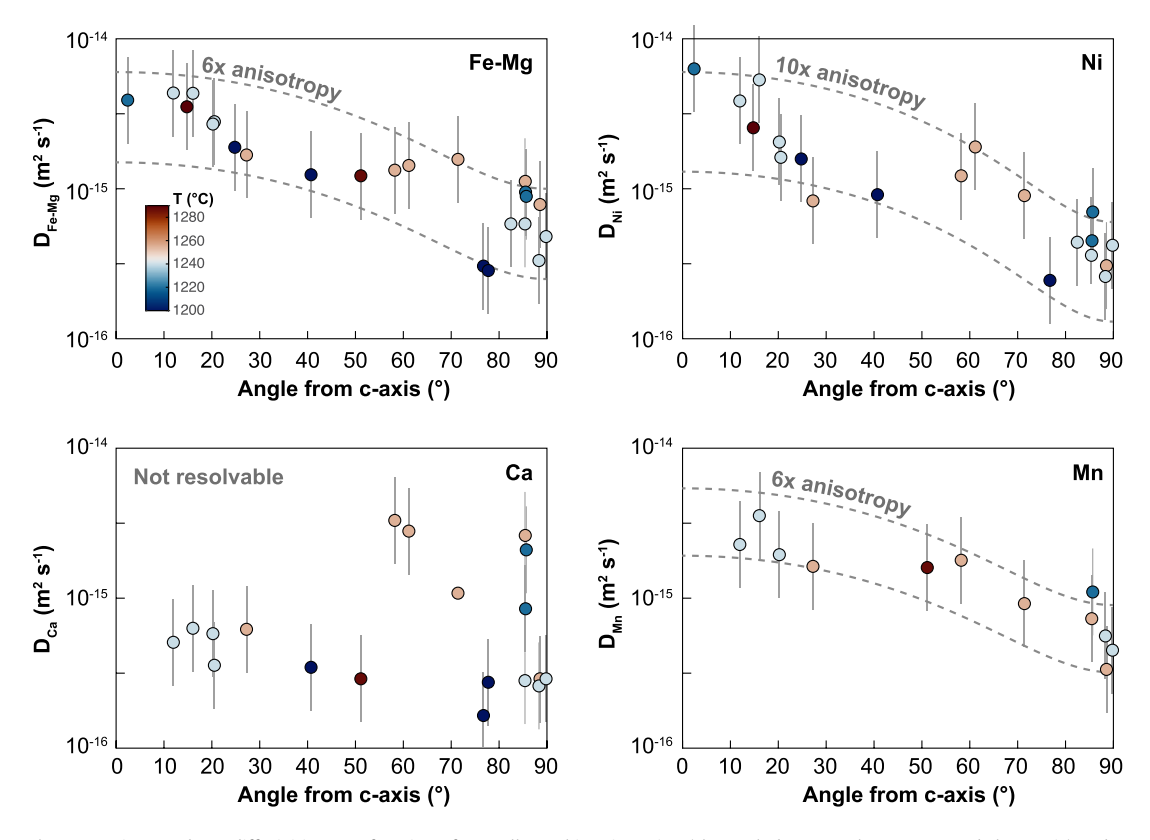


Fig. 7. Experimental Fe-Mg, Ni, Ca and Mn diffusivities as a function of crystallographic orientation (the angle between the traverse and the c-axis) and temperature (color-coded). Dotted gray lines show bounds encompassed by data, with their curvature controlled by magnitude of anisotropy. Fe-Mg, Ni, and Mn all show anisotropy consistent with diffusion being 6–10× faster along the c-axis compared to a or b. Ca does not show consistent anisotropy within the precision of the data. Vertical error bars account for uncertainties in modeling carried out to extract diffusivities and cover a range of 0.6 log units.

ferences of $5\times$, $3.4\times$ and $4.3\times$ for each element), insufficient to account for the order of magnitude differences observed. We note that certain profiles yielded a better fit (lower RMSD) with a onestep model. Additionally, certain profiles could not be fit at all using 2-step models but were well matched by simple 1-step models (e.g., Ca in ol25, compare Fig. 4 and Fig. A5). A number of profiles (k1820_ol20) also yielded the same or higher diffusivities under the two-step assumption, likely because diffusion mostly occurred during the second cooling step (e.g., k1820_ol18, k1820_ol2, k1820_ol26, Fig. A6). In all cases, the premise that concentration gradients formed both during the annealing and after the cooling stage did not result in modeled diffusivities that were low enough to explain the discrepancies between our experiments and solidsolid couples. Maximizing the amount of diffusion that could have occurred during superliquidus treatment does not result in significantly different diffusivities after rim growth and equilibration at the final temperatures. We therefore reject Hypothesis 2 as a reasonable explanation for our different results.

4.3. Hypothesis 3: diffusivities are enhanced by the presence of growthor dissolution-related planar defects

Several studies have shown that cation diffusivities can be enhanced by the presence of extended planar or tube defects (O in titanite, Zhang et al., 2007; Ti in olivine Burgess and Cooper, 2013; Fe-Mg in olivine, Chakraborty et al., 2016; Zr in rutile, Verberne et al., 2022). These extended defects may act as fast diffusion pathways, therefore resulting in greater diffusivities than crystals that are free of those types of defects. We examined whether similar dislocations and/or tube defects could have played a role in increasing cation diffusivities in our experiments. Dislocations could potentially form as a result of interface reaction during dissolution at the initial conditions or during rapid disequilibrium growth

of rims around pre-existing seeds. To explore this possibility, we carried out a TEM investigation of two experimental olivine from our series. A first 10 µm-wide foil was extracted using a focused ion beam scanning electron microscope (FIB-SEM) within a crystal showing rounded edges that was quenched after 24 h at the superliquidus conditions (k1820_ol23). The foil was extracted across the olivine-glass interface (Fig. 8). A second foil was removed at the boundary between seed and overgrowth rim in the shortest experiment (6 hr at 1220 °C, or $\Delta T = 60$ °C) to look for planar defects on either the seed or the rapidly grown rim side. The first foil revealed a \sim 20 nm transitional region between the olivine seed and the glass consisting of discontinuous layers of well-structured olivine without apparent planar defects, and unstructured glass (Fig. 8). While this would presumably be a region of enhanced cation diffusivity, its width is far too narrow to account for the production of concentration gradients several tens of microns in size. The second foil resulted only in perfect olivine lattices both on the seed and rim side, again without evidence for planar or tube defects in TEM imaging. To determine whether dislocations played a role on the larger scale, we also acquired EBSD maps in several grains from our experimental series. Dislocations of a degree or less can be resolved with this technique. Both in smaller and larger high-Fo seeds, EBSD maps clearly resolve a number of dislocations associated with slightly misoriented lattices (Fig. 8). This is particularly prominent in a large San Carlos seed. In both cases, no significant changes in the length of concentration gradients could be measured at and away from those dislocations (See Supplementary Fig. A5). Given these nanoscale (TEM) and microscale (EBSD) observations, we conclude that on a scale relevant to concentration gradients observed in the experimental charges (10 or more microns), planar and tube defects are unlikely to have played a role

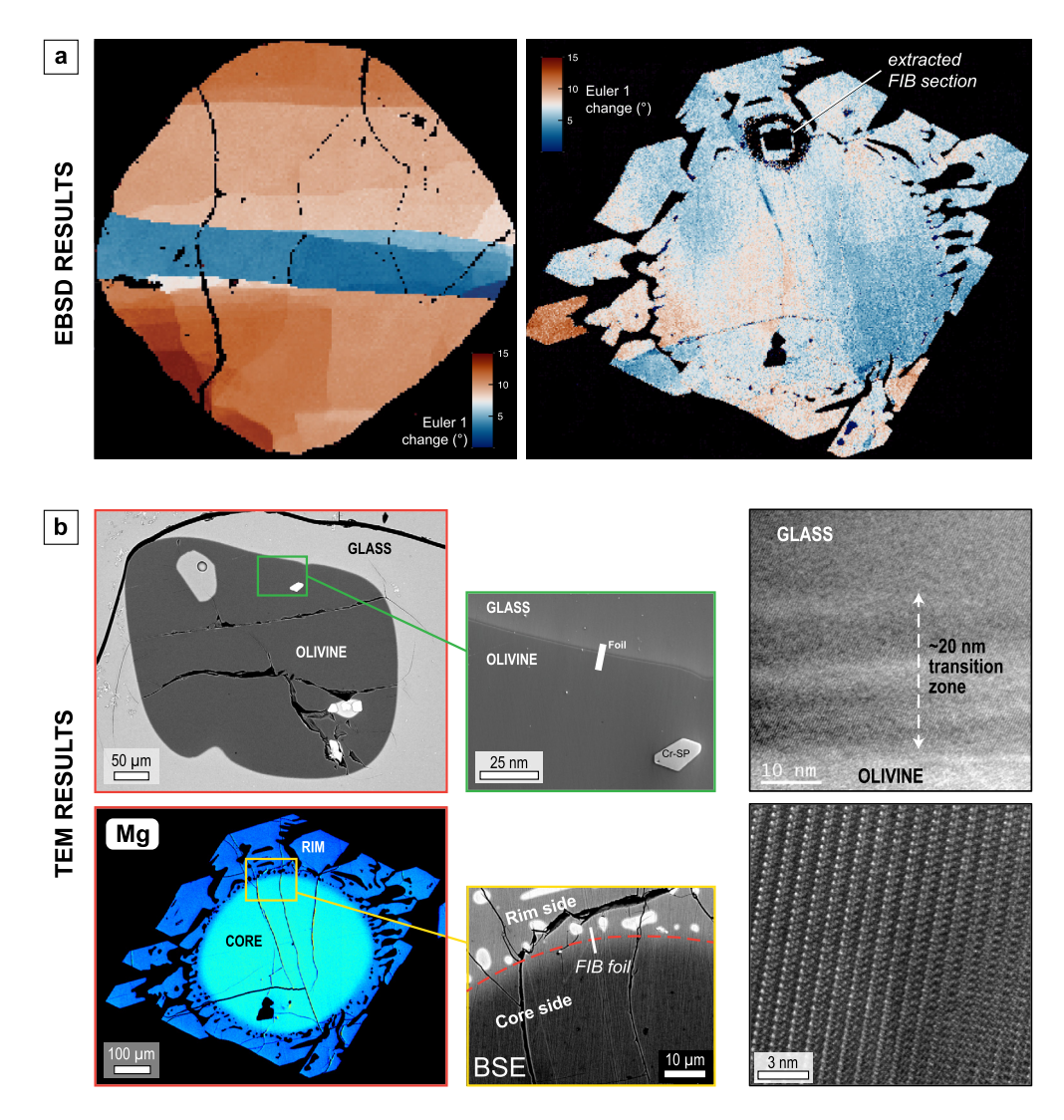


Fig. 8. Search for tube defects or planar dislocations at the micro- and nanoscopic level. (a) EBSD maps in a San Carlos olivine seed (left) and in a natural Kīlauea seed (right) showing dislocation planes in the experimental crystals. These dislocations, however, are uncorrelated with the length of concentration profiles measured (see text and Supplementary Figures). (b) FIB sections were collected in a dissolving (top) and crystallizing (bottom) olivine at the glass-crystal and rim-core interfaces, respectively. In both cases, STEM atomic-resolution darkfield imaging failed to detect any planar or tube dislocations (bottom right). The crystal-melt interface shows a transitional region of ~ 20 nm with well ordered olivine and no order that could form a region of enhanced diffusivity. However, this region is several orders of magnitude too thin (20 nm) to account for the length of concentration gradients measured (tens of microns).

in enhancing cation diffusivities when compared to experimental olivine from other studies in the literature.

4.4. Hypothesis 4: diffusivities are enhanced by the chemistry of the surrounding melt and/or point defects

In the absence of any solid evidence for significant growth-induced contributions to zoning in the diffusion experiments, the likely minor effect of diffusion during the initial dissolution stage, the absence of planar or tube defects resolved at the µm scale, and without any correlation between detected planar dislocations at the crystal scale, we are left with the more likely scenario that an enhanced point defect population catalyzes diffusion of octahedral cations in olivine. Unlike planar or tube defects, point defects are not readily resolvable by TEM or EBSD analysis and thus subject to additional speculation.

There are various ways in which a modified point defect population may affect cation diffusivity in metal sites, but any plausible mechanism must account for the enhanced diffusivities observed in our experiments as well as those of Jurewicz and Watson (1988), and to some degree Spandler and O'Neill (2010), but not in most

other studies involving solid-solid couples. A natural extrapolation of results from these and our studies is that the presence of melt somehow increases diffusion in the lattice. The hypothesis that melt better wets the olivine surface and, in practice, provides unlimited supply of cations compared to powder or thin film sources does not offer a valid explanation for this discrepancy. The diffusant source boundary conditions mainly control the abundance of cations as a function of partitioning laws between the diffusion couple, but do not necessarily affect their mobility. If melt or another agent is responsible for important differences in diffusivities, the underlying mechanisms have to exert an influence on the nature and concentration of point defects.

To understand the effects of different chemical components entering the olivine structure on cation diffusivities, it is necessary to examine their influence on metal site vacancies. This is because the cations studied here are expected to move by exchange with vacant octahedral M-sites. In the following analysis, we assume that arrival of components to the olivine interface is not kinetically hindered – i.e., that these components are in high abundance in the melt around the crystal. We focus on the fayalitic com-

ponent of olivine since it exerts a major control on the vacancy concentration, but the following equations could be rewritten to add a forsteritic component as well. Formation of vacancies can be achieved simply by oxidation of Fe²⁺ to Fe³⁺ on the octahedral site (Nakamura and Schmalzried, 1983; Kohlstedt and Mackwell, 1998; Dohmen and Chakraborty, 2007):

$$2Fe_2^{2+}SiO_4 + SiO_2(m) + O_2(g) = 3Fe_{4/3}^{3+}\square_{2/3}SiO_4$$
 (1a)

The symbol \square denotes a vacancy, in this case on the metal site, and (g) refers to a gas phase while (m) refers to the melt phase here.

In Kröger-Vink notation, this equation is written:

$$6Fe_{M}^{\times} + SiO_{2}(m) + O_{2}(g) = 2V_{M}'' + 4Fe_{M}^{\bullet} + Fe_{2}SiO_{4}$$
 (1b)

In this notation, structural units of crystals X_y^z are defined by the species/element/defect X (V italicized is used for vacancies), the crystallographic site y (e.g., Si for tetrahedral site, M for metal vacancy or octahedral site, i for interstitial), and the charge z relative to the ideal crystal. If there is not charge excess or deficit, z takes on the symbol \times (e.g., Fe_M^\times for Fe^{2+} on its normal octahedral metal site), while positive and negative charges with respect to the ideal crystal are noted $^{\bullet}$ and ' (e.g., Fe_{Si}' for Fe^{3+} on a tetrahedral 'silicon' site).

The product side of Eq. (1) is associated with the charge neutrality condition:

$$\left[\mathsf{Fe}_{\mathsf{M}}^{\bullet}\right] = 2\left[V_{\mathsf{M}}^{"}\right] \tag{1c}$$

where square brackets mean concentration of the defect species per mole olivine.

Assuming that vacancies can be readily incorporated in the lattice at the interface through reaction (1), their diffusion through the crystal can proceed through simple exchange with adjacent atoms of $\mathrm{Fe^{2+}}$ or $\mathrm{Mg^{2+}}$, mediated by Fe redox reactions. Diffusion and distribution of vacancies should be much faster than cation diffusion in our experiments, occurring in < 2 min at the lowest temperature investigated (1200 °C) and along the slow diffusion direction [001] (Kohlstedt and Mackwell, 1998; Demouchy and Mackwell, 2006; Li et al., 2022). While the reaction described by Eq. (1) adequately explains the formation of vacancies in olivine under fO_2 conditions applicable to most magmas, it does not adequately explain why melt-bearing and melt-free systems would lead to different cation diffusivities. We consider four ways in which the presence of melt may affect vacancy concentration and diffusion within the lattice:

- (1) Melt could exert a higher silica activity (aSiO₂, left side of Eq. (1)) than mineral assemblages (olivine, enstatite, periclase) or thin films (e.g., Dohmen et al., 2007) typically used to buffer aSiO₂ in many solid-solid experiments. Increasing aSiO₂ leads to formation of additional M-site vacancies that lead to higher diffusivities of M-site atoms (Zhukova et al., 2014, 2017; Muir et al., 2020; Jollands et al., 2020b). However, MELTS models (Gualda et al., 2012) carried out to calculate aSiO₂ in basalt melt with the same composition as the experimental starting material co-existing with olivine reveal that aSiO₂ is not so different than in olivine-olivine experiments buffered by enstatite, and even possibly lower (aSiO₂ ~ 0.4–0.6 in MELTS models, aSiO₂ ~ 0.6–0.7 in enstatite-olivine experiments, e.g., Zhukova et al., 2014). We therefore conclude that aSiO₂ is unlikely the cause of higher diffusivities in our experiments.
- (2) Natural basalt melt contains numerous elements (e.g., Ti, Al, Na, K, etc.) that are incompatible and in trace amounts in olivine, and thus usually in much higher abundance in melt-olivine couples than in solid-solid configurations. Among

those, Al is a particularly interesting contender because its concentration in melt is three orders of magnitude higher than in the olivine (e.g., Shea et al., 2019). Al is known to diffuse via two different site-specific mechanisms (Zhukova et al., 2017): a dominant, slow-diffusing regime on the T-site and a much faster mechanism mediated by Al on the M-site. In the latter case, Al³⁺ may be incorporated on a M-site at the interface by the crystallization reaction:

$$2Al_2O_3(m) + 3SiO_2(m) = 3Al_{4/3}^{3+} \square_{2/3}SiO_4$$
 (2a)

Or, in Kröger-Vink notation:

$$2Al_2O_3(m) + 3SiO_2(m) = 2V_M'' + 4Al_M^{\bullet}$$
 (2b)

With the charge neutrality condition:

$$\left[\mathsf{Al}_{\mathsf{M}}^{\bullet}\right] = 2\left[V_{\mathsf{M}}^{\prime\prime}\right] \tag{2c}$$

This reaction implies that aAl₂O₃ will strongly influence the formation of vacancies, but only when Al is incorporated into the octahedral site. In reality, Al is more commonly incorporated into the tetrahedral (Si) site, where Mg^{2+} and Si^{4+} are substituted for 2 Al^{3+} . Unlike with Eq. (2), incorporation of Al in the tetrahedral site does not directly lead to formation of octahedral vacancies, and its diffusion is too slow to influence cation diffusion on neighboring M-sites. Nonetheless, as little as tens of ppms of Al present in the octahedral site could have an important effect on metal vacancy concentration (Muir et al., 2020). Cr, in contrast, has comparable concentrations (~ 1000 ppm or less) in melt and olivine (partition coefficient closer to unity) so that it probably influences olivine-olivine and melt-olivine diffusion couples in the same way, and are less likely to lead to the observed differences in M-site-cation diffusivities in melt-bearing and melt-free studies. We note that Cherniak (2010) and Watson et al. (2015) used Al-rich solid powder sources in their studies of REE and P diffusion in olivine and obtained relatively slow diffusivities in both cases. Direct comparisons are, however, difficult because divalent cation diffusivities were not measured.

We also note that boundary layers enriched in incompatible (e.g., Al) or other elements less abundant in olivine than melt (Si) typically form in the melt surrounding rapidly grown olivine and their increased activity could possibly affect defect formation at the interface. However, these enrichments are < 10% relative to the far field composition (Shea et al., 2019) and will not increase aAl₂O₃ or aSiO₂ to a significant enough degree. While boundary layers may exert a minor influence on defect formation at the interface, they cannot explain the order of magnitude difference in diffusivities observed.

(3) Natural basalt melt contains a substantial amount of water, even at 1-atm conditions (e.g., ~ 1000 ppm). Under hydrous conditions, with contribution of a $\rm H_2O$ component in the melt, another major defect type involves the creation of vacancies on the metal site by incorporation of OH groups in the olivine structure. One possible reaction is:

$$Fe_2^{2+}SiO_4 + SiO_2(m) + \frac{1}{2}H_2O(fl) + \frac{3}{2}O_2(g) = 2Fe^{3+} \square HSiO_4$$
(3a)

Or, in Kröger-Vink notation:

$$\operatorname{Fe}_{\mathrm{M}}^{x} + \operatorname{SiO}_{2}(m) + \frac{1}{2}\operatorname{H}_{2}\operatorname{O}(fl) + \frac{3}{2}\operatorname{O}_{2}(g) = \operatorname{Fe}_{\mathrm{M}}^{\bullet} + \left\{ (\operatorname{OH})_{\mathrm{O}}^{\bullet} - V_{\mathrm{M}}'' \right\}' \tag{3b}$$

With the charge neutrality condition:

$$\left[\text{Fe}_{\text{M}}^{\bullet} \right] = \left[\left\{ (\text{OH})_{\text{O}}^{\bullet} - V_{\text{M}}'' \right\}' \right] \tag{3c}$$

Comparable reactions have been proposed previously to examine incorporation and intracrystalline diffusion of hydrogen (Kohlstedt and Mackwell, 1998; Demouchy et al., 2007).

Following the same logic as Wang et al. (2004) or Hier-Majumder et al. (2005), extra vacancies formed by significantly increasing the amount of Al or H incorporated at the meltolivine interface should be correlated positively with diffusivity of elements like Fe-Mg. This is usually expressed as:

$$\tilde{D}_{\text{Fe-Mg}} = X_{V_{Ma}'} \cdot \tilde{D}_{V_{Ma}'} \tag{4}$$

Where $\tilde{D}_{\text{Fe-Mg}}$ is the Fe-Mg interdiffusivity, $\tilde{D}_{V_{Me}''}$ the effective vacancy diffusivity, and $X_{V_{Me}''}$ the total concentration of vacancies in the octahedral site. Assuming that vacancies associated with OH, Al_{M}^{\bullet} or Fe_{M}^{\bullet} all contribute to $X_{V_{Me}''}$, Fe-Mg interdiffusion should therefore increase with an increase in their abundance. In our experiments, it is possible that hydrogen is diffusing in or out of the olivine, depending on the natural setting in which they crystallized. San Carlos is likely drier than Kīlauea olivine, and the latter may have crystallized in a more H_2O -rich melt than our experiments. Despite these differences in H concentration, both types of olivine yield the same order-of-magnitude higher diffusivities than prior studies utilizing dry solid-solid couples. Most likely, it is the final, equilibrium vacancy concentration that influences cation diffusion more than the short-term directionality of hydrogen diffusion.

(4) Rapid olivine growth results in higher and/or non-equilibrium point defect concentrations. Our TEM and EBSD investigation failed to reveal planar or other defects within both the core and rapidly grown rims of olivine. It is, however, possible that rapid crystal growth sets - or resets - the concentration of various point defects by incorporating trace elements in higher, disequilibrium concentrations (e.g., Watson and Müller, 2009; Shea et al., 2019). Two indirect lines of evidence suggest rapid growth is not necessary to lead to higher diffusivities: (a) Spandler and O'Neill (2010) obtained high cation diffusivities in melt-olivine experiments devoid of growth at the interface; (b) Our experiments guenched at superliquidus temperatures (ol23 and ol27, Table 1) yielded diffusivities much higher than predicted by the literature, exceeding dissolution rates, and without experiencing growth. These results do not ultimately imply that rapid growth has no effect on cation diffusivities, but rather that it is not a sine qua non condition for fast diffusion.

Future studies will hopefully shed light on which of these point-vacancy-forming mechanisms is most likely to affect M-site cation diffusivities. The full contribution of Al will be difficult to constrain experimentally, given the challenges in isolating the effect of aSiO₂ from aAl₂O₃ and in distinguishing the far less abundant octahedrally coordinated Al from tetrahedral Al. In contrast, pinpointing the relative influence of H may be more tractable given that hydrogen concentration can be controlled independently via changes in experimental pressure and/or oxygen fugacity. The effect of rapid growth on defect concentration and cation diffusivities will in turn require series of experiments comparing reaction-free and overgrown melt-olivine interfaces.

5. Implications for diffusion chronometry

Disagreements between experimentally-derived element diffusivities are relatively common and can originate from differences in the experimental and/or analytical approach used, or complex

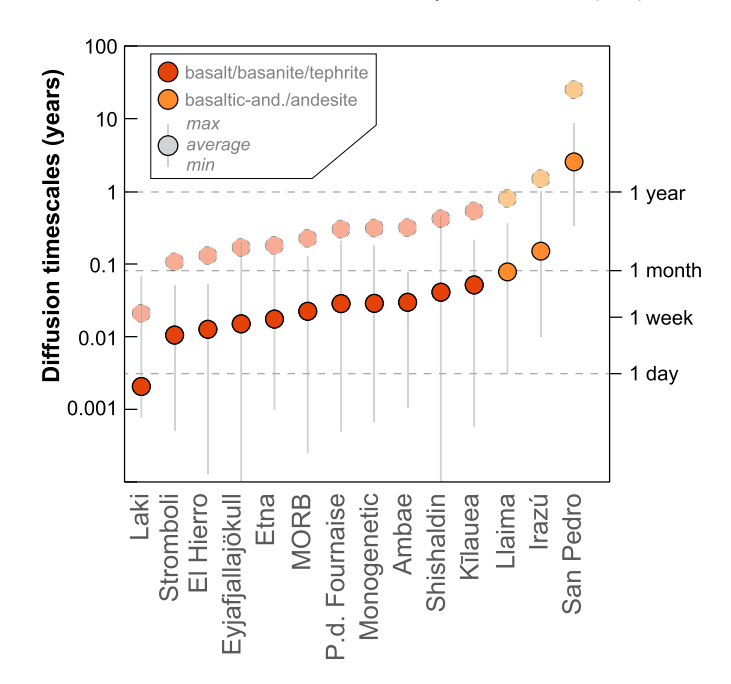


Fig. 9. The effect of underestimating diffusion rates by a factor of 10 on timescales associated with magmatic processes (e.g., mixing-to-eruption) at basaltic and andesitic volcanoes (modified from Costa et al., 2020). Timescales that were previously thought to represent processes occurring over \sim 1-month to 1-yr periods would be shifted to \sim 1-day to \sim 1-month.

multi-site diffusion behavior (e.g., Cherniak, 2010 and Spandler and O'Neill, 2010 for REE in olivine; Allan et al., 2013 and Dohmen et al., 2016 for Fe-Mg in opx; Cherniak et al., 2007 and Jollands et al., 2020a for Ti in quartz; see also Dohmen et al., 2010 for multi-site Li diffusion in olivine). Some of these discrepancies in olivine were acknowledged and discussed (see Chakraborty, 2010 for a review) but their origins have remained puzzling. Our results show that, similar to Jurewicz and Watson (1988) and Spandler and O'Neill (2010), experiments that involve melt-bearing configurations tend to yield higher diffusivities. Applications of diffusion chronometry focused on the timescales of magmatic processes may thus need to be revisited. Cation diffusivities examined here (Fe-Mg, Ni, Mn, and to a lesser extent Ca) are 10 times faster than in melt-free systems, meaning that timescales obtained from modeling natural concentration profiles may be 10 times shorter than the values published. If true, interpreting and correlating these timescales in the context of pre-eruptive unrest sequences and other datasets (e.g., seismicity, deformation, gas release, changes in melt inclusion trapping depths) will also require reexamination. Fig. 9 shows the effects of shortening the timescale compilation of Costa et al. (2020) by a factor of 10. Pre-eruptive magmatic timescales previously recorded perturbations generally occurring on timeframes of a month to a few years. These perturbations to the magmatic system would have occurred days to a month prior to eruption using faster diffusion rates.

6. Conclusions

Diffusion experiments involving melt-olivine couples have so far yielded faster diffusion rates for major and minor elements compared to experiments that use olivine-olivine, thin film-olivine or powder-olivine couples. Interface reactions (growth, dissolution) or the lack of a perfect interface geometry in our seeded experiments cannot reasonably explain the order of magnitude difference in measured diffusivities. Other planar, dislocation-related or 'tube' defects previously suggested to enhance diffusion are absent or uncorrelated with concentration gradients. We conclude that

point defects, presumably additional vacancies created at or near the melt-olivine interface, are likely responsible for the higher diffusivities. Elements that are in far higher concentration in melts compared to most solid diffusant sources (e.g., Al, Ti, Na, H) may be involved in vacancy-forming reactions as they are incorporated as trace elements in the olivine lattice. For applications of diffusion chronometry that involve melt-rich magmatic systems, confirming these results and targeting the specific reactions involved in catalyzing diffusivities will be critical. The next generation of olivine diffusion experiments could expand and generalize the use of olivine crucible configurations with well controlled interface geometries (Spandler and O'Neill, 2010) to derive revised cation diffusivities. In the meantime, we recommend that studies utilizing concentration gradients in Fe-Mg, Mn, Ni or Ca to extract timescales continue to use values from solid-solid couples but consider the possibility of an order of magnitude change and the consequences for pre-eruptive processes on a case-by-case basis.

CRediT authorship contribution statement

Thomas Shea: Writing – review & editing, Writing – original draft, Methodology, Investigation, Funding acquisition, Formal analysis, Conceptualization. **Dawn Ruth:** Writing – review & editing, Resources, Methodology, Formal analysis. **Michael Jollands:** Writing – review & editing, Methodology, Investigation. **Kenta Ohtaki:** Software, Methodology, Formal analysis. **Hope Ishii:** Writing – review & editing, Methodology, Investigation, Formal analysis. **John Bradley:** Writing – review & editing, Methodology, Investigation, Formal analysis.

Declaration of competing interest

The authors declare that they have no known competing financial interests or personal relationships that could have appeared to influence the work reported in this paper.

Data availability

Data will be made available on request.

Acknowledgements

NSF EAR-1725321 and EAR-2047313 grants supported this work. The authors thank Megan Newcombe, one anonymous reviewer, and Kendra Lynn (USGS Internal Review) for the helpful questions and suggestions, as well as Sumit Chakraborty and Ralf Dohmen for the numerous discussions and input on defects in olivine. We also thank Chiara Maria Petrone for thorough and swift editorial handling of the manuscript. Any use of trade, firm, or product names is for descriptive purposes only and does not imply endorsement by the U.S. Government.

Appendix A. Supplementary material

Supplementary material related to this article can be found online at https://doi.org/10.1016/j.epsl.2023.118370.

References

- Albert, H., Costa, F., Martí, J., 2015. Timing of magmatic processes and unrest associated with mafic historical monogenetic eruptions in Tenerife island. J. Petrol. 56, 1945–1966. https://doi.org/10.1093/petrology/egv058.
- Albert, H., Costa, F., Di Muro, A., Herrin, J., Métrich, N., Deloule, E., 2019. Magma interactions, crystal mush formation, timescales, and unrest during caldera collapse and lateral eruption at ocean island basaltic volcanoes (Piton de la Fournaise, La Réunion). Earth Planet. Sci. Lett. 515, 187–199. https://doi.org/10.1016/j.epsl.2019.02.035.

- Allan, A.S.R., Morgan, D.J., Wilson, C.J.N., Millet, M.-A., 2013. From mush to eruption in centuries: assembly of the super-sized Oruanui magma body. Contrib. Mineral. Petrol. 166, 143–164. https://doi.org/10.1007/s00410-013-0869-2.
- Burgess, K.D., Cooper, R.F., 2013. Extended planar defects and the rapid incorporation of Ti⁴⁺ into olivine. Contrib. Mineral. Petrol. 166, 1223–1233. https://doi.org/10.1007/s00410-013-0918-x.
- Caracciolo, A., Kahl, M., Bali, E., Guðfinnsson, G.H., Halldórsson, S.A., Hartley, M.E., 2021. Timescales of crystal mush mobilization in the Bárðarbunga-Veiðivötn volcanic system based on olivine diffusion chronometry. Am. Mineral. 106, 1083–1096. https://doi.org/10.2138/am-2021-7670.
- Chakraborty, S., 1997. Rates and mechanisms of Fe-Mg interdiffusion in olivine at 980°-1300°C. J. Geophys. Res. 102, 12317-12331. https://doi.org/10.1029/97IB00208.
- Chakraborty, S., 2008. Diffusion in solid silicates: a tool to track timescales of processes comes of age. Annu. Rev. Earth Planet. Sci. 36, 153–190. https:// doi.org/10.1146/annurev.earth.36.031207.124125.
- Chakraborty, S., 2010. Diffusion coefficients in olivine, wadsleyite and ringwoodite. Rev. Mineral. Geochem. 72, 603–639. https://doi.org/10.2138/rmg.2010.72.13.
- Chakraborty, S., Marquardt, K., Bobrowski, H., 2016. The connection between diffusion, dissolution, deformation and evaporation: the role of mobile dislocations. In: AGU Fall Meeting Abstracts, pp. MR42A-05.
- Chen, Y., Zhang, Y., 2008. Olivine dissolution in basaltic melt. Geochim. Cosmochim. Acta 72, 4756–4777. https://doi.org/10.1016/j.gca.2008.07.014.
- Cherniak, D.J., 2010. REE diffusion in olivine. Am. Mineral. 95, 362–368. https://doi. org/10.2138/am.2010.3345.
- Cherniak, D.J., Watson, E.B., Wark, D.A., 2007. Ti diffusion in quartz. Chem. Geol. 236, 65–74. https://doi.org/10.1016/j.chemgeo.2006.09.001.
- Coogan, L.A., Hain, A., Stahl, S., Chakraborty, S., 2005. Experimental determination of the diffusion coefficient for calcium in olivine between 900°C and 1500°C. Geochim. Cosmochim. Acta 69, 3683–3694. https://doi.org/10.1016/j.gca.2005.
- Costa, F., Dohmen, R., Chakraborty, S., 2008. Time scales of magmatic processes from modeling the zoning patterns of crystals. Rev. Mineral. Geochem. 69, 545–594. https://doi.org/10.2138/rmg.2008.69.14.
- Costa, F., Shea, T., Ubide, T., 2020. Diffusion chronometry and the timescales of magmatic processes. Nat. Rev. Earth Environ. 1, 201–214. https://doi.org/10.1038/s43017-020-0038-x.
- Demouchy, S., Mackwell, S., 2006. Mechanisms of hydrogen incorporation and diffusion in iron-bearing olivine. Phys. Chem. Miner. 33, 347–355. https://doi.org/10.1007/s00269-006-0081-2.
- Demouchy, S., Mackwell, S.J., Kohlstedt, D.L., 2007. Influence of hydrogen on Fe–Mg interdiffusion in (Mg,Fe)O and implications for Earth's lower mantle. Contrib. Mineral. Petrol. 154, 279–289. https://doi.org/10.1007/s00410-007-0193-9.
- Dohmen, R., Becker, H.-W., Chakraborty, S., 2007. Fe–Mg diffusion in olivine I: experimental determination between 700 and 1,200 °C as a function of composition, crystal orientation and oxygen fugacity. Phys. Chem. Miner. 34, 389–407. https://doi.org/10.1007/s00269-007-0157-7.
- Dohmen, R., Chakraborty, S., 2007. Fe–Mg diffusion in olivine II: point defect chemistry, change of diffusion mechanisms and a model for calculation of diffusion coefficients in natural olivine. Phys. Chem. Miner. 34, 409–430. https://doi.org/10.1007/s00269-007-0158-6.
- Dohmen, R., Kasemann, S.A., Coogan, L., Chakraborty, S., 2010. Diffusion of Li in olivine. Part I: experimental observations and a multi species diffusion model. Geochim. Cosmochim. Acta 74, 274–292. https://doi.org/10.1016/j.gca.2009.10.
- Dohmen, R., Ter Heege, J.H., Becker, H.-W., Chakraborty, S., 2016. Fe-Mg interdiffusion in orthopyroxene. Am. Mineral. 101, 2210–2221. https://doi.org/10.2138/am-2016-5815.
- Garcia, M.O., Pietruszka, A.J., Rhodes, J.M., 2003. A petrologic perspective of Kīlauea volcano's summit magma reservoir. J. Petrol. 44, 2313–2339. https://doi.org/10.1093/petrology/egg079.
- Gavrilenko, M., Batanova, V.G., Llovet, X., Krasheninnikov, S., Koshlyakova, A.N., Sobolev, A.V., 2023. Secondary fluorescence effect quantification of EPMA analyses of olivine grains embedded in basaltic glass. Chem. Geol. 621, 121328. https://doi.org/10.1016/j.chemgeo.2023.121328.
- Gualda, G.A.R., Ghiorso, M.S., Lemons, R.V., Carley, T.L., 2012. Rhyolite-MELTS: a modified calibration of MELTS optimized for silica-rich, fluid-bearing magmatic systems. J. Petrol. 53, 875–890. https://doi.org/10.1093/petrology/egr080.
- Hier-Majumder, S., Anderson, I.M., Kohlstedt, D.L., 2005. Influence of protons on Fe-Mg interdiffusion in olivine. J. Geophys. Res., Solid Earth 110. https://doi.org/10.1029/2004/B003292.
- Holzapfel, C., Chakraborty, S., Rubie, D.C., Frost, D.J., 2007. Effect of pressure on Fe–Mg, Ni and Mn diffusion in (Fe_xMg_{1-x})₂SiO₄ olivine. Phys. Earth Planet. Inter. 162, 186–198. https://doi.org/10.1016/j.pepi.2007.04.009.
- Ito, M., Ganguly, J., 2006. Diffusion kinetics of Cr in olivine and ⁵³Mn-⁵³Cr thermochronology of early solar system objects. Geochim. Cosmochim. Acta 70, 799-809. https://doi.org/10.1016/j.gca.2005.09.020.
- Jollands, M.C., Bloch, E., Müntener, O., 2020a. New Ti-in-quartz diffusivities reconcile natural Ti zoning with time scales and temperatures of upper crustal magma reservoirs. Geology 48, 654–657. https://doi.org/10.1130/G47238.1.

- Jollands, M.C., Zhukova, I., O'Neill, H.St.C., Hermann, J., 2020b. Mg diffusion in forsterite from 1250–1600 °C. Am. Mineral. 105, 525–537. https://doi.org/10. 2138/am-2020-7286.
- Jurewicz, A.J.G., Watson, E.B., 1988. Cations in olivine, Part 2: diffusion in olivine xenocrysts, with applications to petrology and mineral physics. Contrib. Mineral. Petrol. 99, 186–201. https://doi.org/10.1007/BF00371460.
- Kahl, M., Chakraborty, S., Costa, F., Pompilio, M., Liuzzo, M., Viccaro, M., 2013. Compositionally zoned crystals and real-time degassing data reveal changes in magma transfer dynamics during the 2006 summit eruptive episodes of Mt. Etna. Bull. Volcanol. 75, 692. https://doi.org/10.1007/s00445-013-0692-7.
- Kent, A.J.R., 2008. Melt inclusions in basaltic and related volcanic rocks. Rev. Mineral. Geochem. 69, 273–331. https://doi.org/10.2138/rmg.2008.69.8.
- Kohlstedt, D.L., Mackwell, S.J., 1998. Diffusion of hydrogen and intrinsic point defects in olivine. Z. Phys. Chem. 207, 147–162. https://doi.org/10.1524/zpch.1998.207. Part 1 2.147.
- Lambart, S., Hamilton, S., Lang, O.I., 2022. Compositional variability of San Carlos olivine. Chem. Geol. 605, 120968. https://doi.org/10.1016/j.chemgeo.2022. 120968
- Lasaga, A.C., 1982. Toward a master equation in crystal growth. Am. J. Sci. 282, 1264. https://doi.org/10.2475/ais.282.8.1264.
- Li, Y., Mackwell, S.J., Kohlstedt, D.L., 2022. Diffusion rates of hydrogen defect species associated with site-specific infrared spectral bands in natural olivine. Earth Planet. Sci. Lett. 581, 117406. https://doi.org/10.1016/j.epsl.2022.117406.
- Longpré, M.-A., Klügel, A., Diehl, A., Stix, J., 2014. Mixing in mantle magma reservoirs prior to and during the 2011–2012 eruption at El Hierro, Canary Islands. Geology 42, 315–318. https://doi.org/10.1130/G35165.1.
- Lynn, K.J., Garcia, M.O., Shea, T., Costa, F., Swanson, D.A., 2017. Timescales of mixing and storage for Keanakāko'i Tephra magmas (1500–1820 C.E.), Kīlauea Volcano, Hawai'i. Contrib. Mineral. Petrol. 172, 76. https://doi.org/10.1007/s00410-017-1395-4.
- Mourey, A.J., Shea, T., 2019. Forming olivine phenocrysts in basalt: a 3D characterization of growth rates in laboratory experiments. Front. Earth Sci. 7, 300. https://doi.org/10.3389/feart.2019.00300.
- Muir, J.M.R., Jollands, M., Zhang, F., Walker, A.M., 2020. Explaining the dependence of M-site diffusion in forsterite on silica activity: a density functional theory approach. Phys. Chem. Miner. 47, 55. https://doi.org/10.1007/s00269-020-01123-5
- Nakamura, A., Schmalzried, H., 1983. On the nonstoichiometry and point defects of olivine. Phys. Chem. Miner. 10, 27–37. https://doi.org/10.1007/BF01204323.
- Pankhurst, M.J., Morgan, D.J., Thordarson, T., Loughlin, S.C., 2018. Magmatic crystal records in time, space, and process, causatively linked with volcanic unrest. Earth Planet. Sci. Lett. 493, 231–241. https://doi.org/10.1016/j.epsl.2018.04.025.
- Petry, C., Chakraborty, S., Palme, H., 2004. Experimental determination of Ni diffusion coefficients in olivine and their dependence on temperature, composition, oxygen fugacity, and crystallographic orientation. Geochim. Cosmochim. Acta 68, 4179–4188. https://doi.org/10.1016/j.gca.2004.02.024.
- Rasmussen, D.J., Plank, T.A., Roman, D.C., Power, J.A., Bodnar, R.J., Hauri, E.H., 2018. When does eruption run-up begin? Multidisciplinary insight from the 1999 eruption of Shishaldin volcano. Earth Planet. Sci. Lett. 486, 1–14. https://doi.org/10.1016/j.epsl.2018.01.001.

- Ruth, D.C.S., Costa, F., Bouvet de Maisonneuve, C., Franco, L., Cortés, J.A., Calder, E.S., 2018. Crystal and melt inclusion timescales reveal the evolution of magma migration before eruption. Nat. Commun. 9, 2657. https://doi.org/10.1038/s41467-018-05086-8.
- Shea, T., Costa, F., Krimer, D., Hammer, J.E., 2015. Accuracy of timescales retrieved from diffusion modeling in olivine: a 3D perspective. Am. Mineral. 100, 2026–2042.
- Shea, T., Hammer, J.E., Hellebrand, E., Mourey, A.J., Costa, F., First, E.C., Lynn, K.J., Melnik, O., 2019. Phosphorus and aluminum zoning in olivine: contrasting behavior of two nominally incompatible trace elements. Contrib. Mineral. Petrol. 174, 85. https://doi.org/10.1007/s00410-019-1618-y.
- Shea, T., Matzen, A.K., Mourey, A.J., 2022. Experimental study of Fe-Mg partitioning and zoning during rapid growth of olivine in Hawaiian tholeiites. Contrib. Mineral. Petrol. 177, 114. https://doi.org/10.1007/s00410-022-01969-8.
- Spandler, C., O'Neill, H.St.C., 2010. Diffusion and partition coefficients of minor and trace elements in San Carlos olivine at 1,300 °C with some geochemical implications. Contrib. Mineral. Petrol. 159, 791–818. https://doi.org/10.1007/s00410-009-0456-8.
- Verberne, R., van Schrojenstein Lantman, H.W., Reddy, S.M., Alvaro, M., Wallis, D., Fougerouse, D., Langone, A., Saxey, D.W., Rickard, W.D.A., 2022. Trace-element heterogeneity in rutile linked to dislocation structures: implications for Zr-inrutile geothermometry. J. Metamorph. Geol. https://doi.org/10.1111/jmg.12686.
- Viccaro, M., Giuffrida, M., Zuccarello, F., Scandura, M., Palano, M., Gresta, S., 2019. Violent paroxysmal activity drives self-feeding magma replenishment at Mt. Etna. Sci. Rep. 9, 6717. https://doi.org/10.1038/s41598-019-43211-9.
- Wallace, P.J., Plank, T., Bodnar, R.J., et al., 2021. Olivine-hosted melt inclusions: a microscopic perspective on a complex magmatic world. Annu. Rev. Earth Planet. Sci. 49, 465–494. https://doi.org/10.1146/annurev-earth-082420-060506.
- Wang, Z., Hiraga, T., Kohlstedt, D.L., 2004. Effect of H⁺ on Fe-Mg interdiffusion in olivine (Fe, Mg)₂SiO₄. Appl. Phys. Lett. 85, 209-211. https://doi.org/10.1063/1. 1769593
- Watson, E.B., Müller, T., 2009. Non-equilibrium isotopic and elemental fractionation during diffusion-controlled crystal growth under static and dynamic conditions. Chem. Geol. 267, 111–124. https://doi.org/10.1016/j.chemgeo.2008.10.036.
- Watson, E.B., Cherniak, D.J., Holycross, M.E., 2015. Diffusion of phosphorus in olivine and molten basalt. Am. Mineral. 100, 2053–2065. https://doi.org/10.2138/am-2015-5416.
- Zhang, X.Y., Watson, E.B., Cherniak, D.J., 2007. Oxygen self-diffusion "fast-paths" in titanite single crystals and a general method for deconvolving self-diffusion profiles with "tails". Geochim. Cosmochim. Acta 71, 1563–1573. https://doi.org/10. 1016/j.gca.2006.12.013.
- Zhukova, I., O'Neill, H.St.C., Campbell, I.H., Kilburn, M.R., 2014. The effect of silica activity on the diffusion of Ni and Co in olivine. Contrib. Mineral. Petrol. 168, 1029. https://doi.org/10.1007/s00410-014-1029-z.
- Zhukova, I., O'Neill, H.St.C., Campbell, I.H., 2017. A subsidiary fast-diffusing substitution mechanism of Al in forsterite investigated using diffusion experiments under controlled thermodynamic conditions. Contrib. Mineral. Petrol. 172, 53. https://doi.org/10.1007/s00410-017-1365-x.